analytical chemistry

pubs.acs.org/ac Article

Damage-Free and Time-Saving Platform Integrated by a Flow Membrane Separation Device and a Dual-Target Biofuel Cell-Based Biosensor for Continuous Sorting and Detection of Exosomes and Host Cells in Human Serum

Tajiguli Yimamumaimaiti, Qiwen Su, Rong-bin Song, Yan Gao, Sha Yu, Tingting Tan, Linlin Wang,* Jun-Jie Zhu,* and Jian-Rong Zhang*

Cite This: *Anal. Chem.* 2022, 94, 7722−7730 Read Online

ACCESS | Metrics & More | Article Recommendations | Supporting Information

ABSTRACT: The growth relationship between exosomes (EXOs) and the host cells is highly desired for tumor evaluations, which puts forward high demand on the accurate and convenient acquisition of their individual quantitative information. However, the tedious and destructive separation process and the requirement of dual-channel detection make it become an extremely challenging task. Herein, we integrated an enzymatic biofuel cell (EBFC)-powered biosensor with a flow cell-supported membrane separation device (FMSC) to develop a continuous separation and detection platform for EXOs and host cancer cells in human serum. The FMSC equipped with an aluminum oxide membrane served as a size-dependent sorting unit to nondestructively extract EXOs from human serum within 5 min, representing a 99.3% reduction in isolating time compared to ultracentrifugation. The EBFC-powered biosensors modified with different aptamers on anodes and cathodes were used as a dual-channel sensing unit. By regulating the controlling valves of different fluid passages, the extracted EXOs and residual host cells could be successively inputted into EBFC-powered biosensors, which generated a segmental degradation in output performance due to the EXO-and host cell-caused increase in the steric hindrance of anodes and cathodes, respectively. Based on these degradations, we obtained the quantitative information of EXOs and host cells with a record-breaking sensitivity (EXOs: 5.59×10^3 particles/mL and host cells: 25 cells/mL). Moreover, the growth relationship between EXOs and host cells was also built, which would be beneficial for the disclosure of the growth state or even more detailed biology information of tumor.

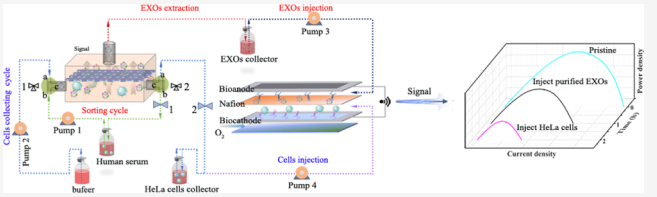

INTRODUCTION

As a special kind of self-secreted extracellular vesicles, exosomes (EXOs) carrying abundant tumor-derived cancerous protein and nucleic acid have become an emerging biomarker for early cancer diagnosis.[1−7] Not only this, it is also revealed that EXOs existing in a tumor microenvironment can regulate the communication between tumor cells and their microenvironment, which plays an important role in the tumor growth and metastasis.[8−11] In this context, we should not only focus on the directive function of EXO analysis on tumor occurrence but also should think about the potential association between EXO quantitative information and tumor growth or even metastasis. To cognize such potential association, a primary demand is to build the growth relationship between EXOs and host cancer cells, which can provide more precious and in-depth information about tumors and the EXO-secreting capability of host cells during different growth periods.[12] Although extensive efforts have been dedicated to develop novel sensing strategies for EXO detection, the simultaneous collection of the quantitative information of EXOs and the host cells that can be conducive to their growth relationship has not been touched yet.

EXOs contain similar surface markers to their host cells, making it extremely difficult to specifically detect them depending solely on the aptamer recognition strategy. The expression level of EXOs in the body fluid is also low.[13] In view of these features, it is necessary to rapidly isolate and concentrate EXOs from the host cell-containing body fluids before detecting them. Ultracentrifugation is the representative and commonly used EXO isolation method. However, ultracentrifugation-based isolation methods are normally time-consuming (>12 h) due to the small size of EXOs (<300 nm). Moreover, the structure of EXOs is easy to be destroyed by the powerful mechanical forces of ultra-

Received: April 16, 2022
Accepted: May 9, 2022
Published: May 19, 2022

https://doi.org/10.1021/acs.analchem.2c01680
Anal. Chem. 2022, 94, 7722−7730

Scheme 1. Schematic Diagram and Working Principle of the FMSC- and EBFC-Powered Biosensor Coupled Sensing System for the Continuous Detection of EXOs and Host HeLa Cells (a) and the Design and Working Principle of EBFC-Powered Biosensor for the Detection of EXOs and Host HeLa Cells (b)

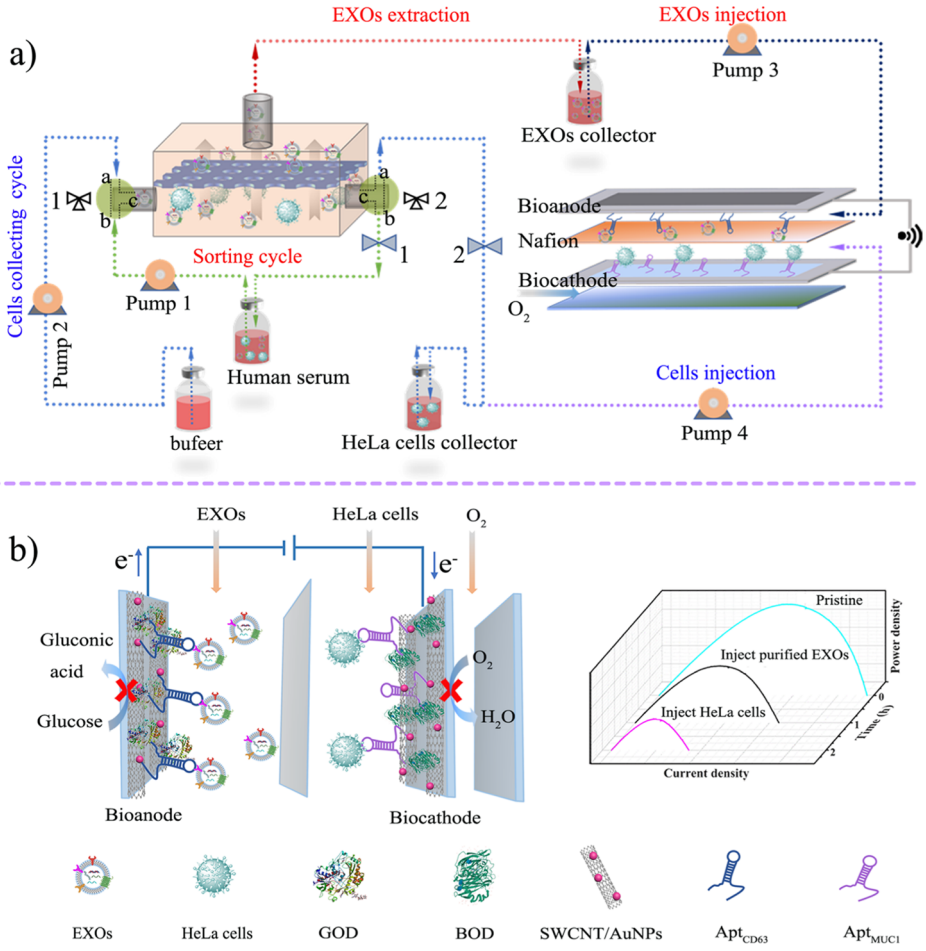

centrifugation, which will bring unpredictable risks in the detection accuracy.[14,15] To address these issues, one promising solution is to employ flow membrane separation technology, which can isolate EXOs from host cells based on the size-sieving function. In addition to its moderate separation manner, circulating the fluid can reduce the time cost of repetitive centrifugation and minimize the introduction of extra fluid to dilute the target solution.

Regarding the sensing part, a general design is to develop two independent detection units for the extracted EXOs and the residual host cells in the body fluid. Obviously, such an arrangement can avoid the interferences between EXOs and host cells, but it also adds complexity and lowers the integration degree between the separation and sensing part. In this case, a dual-channel detection unit with the capability of multi-target analysis is highly desirable. Enzymatic biofuel cell (EBFC)-powered biosensors can provide continuous and real-time signals depending solely on the output changes of EBFCs.[16−20] Because no external power is applied and the enzyme catalytic electrode reactions are highly specific, the EBFC-powered biosensors exhibit outstanding anti-interference capacity and are capable of detecting the targets in situ with high selectivity.[21−23] More importantly, the dual-chamber structure of EBFC-powered biosensors can guarantee independent space for different targets, while the anode and cathode can be designed to capture different targets by modifying corresponding recognition elements. Therefore, we deduced that the EBFC-powered biosensors have the potential to become a dual-channel detection system if the input interval of EXOs and their host cells is well-controlled.

In this study, we developed a damage-free and high-integrity platform to rapid isolate and continuously detect EXOs and host cancer cells for building their growth relationship, by adopting a flow cell-supported membrane separation device (FMSC) as a separation unit and EBFC-powered biosensors as a dual-channel sensing unit. The HeLa cells were taken as the research model. As shown in Scheme 1a, the FMSC was equipped with a porous anodic aluminum oxide membrane (AAO), whose pores were intermediate in size between EXOs and HeLa cells (~350 nm). During the EXO sorting process, the tee valves were set to connect channels b and c, and the human serum could be inputted into the FMSC in a circulation flow mode (green route) with the aid of pump 1. With the adjustment of pressure with a flow speed controller (no. 1), the EXOs (<300 nm) could infiltrate into the upper chamber and the corresponding collector (red route) within 5 min, realizing the EXO isolation by the size sieving effect. The tee valves (nos. 1 and 2) were then set to connect channels a and b for initiating the host cell collection process. The HeLa cells trapped in the lower chamber can be flowed into its collector by the introduction of buffer solution under the drive of pump 2 (blue route). The HeLa cells existing in the bottle of human

https://doi.org/10.1021/acs.analchem.2c01680
Anal. Chem. 2022, 94, 7722−7730

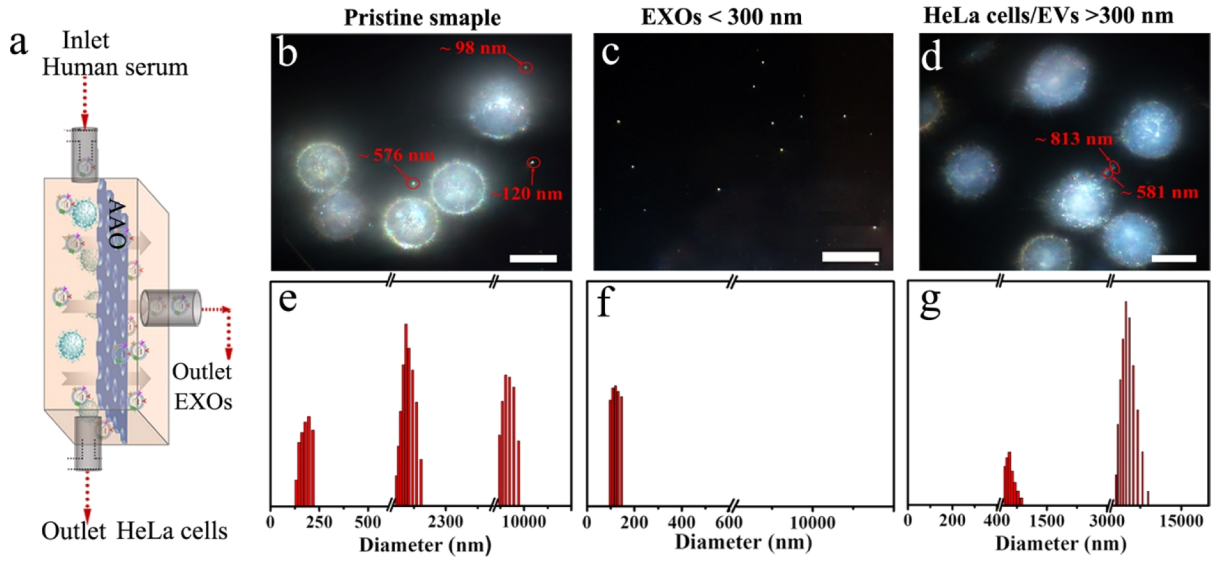

Figure 1. (a) Schematic diagram of the structure and the separation function of the FMSC. The dark-field images (b–d) (Scale bars: 10 μm) and dynamic light scattering results (e–g) of the different systems: pristine human serum (b,e), the purified EXOs (c,f), and the purified HeLa cells (d,g).

serum were transferred into lower chamber of the FMSC and the corresponding collector in succession by repeating the green and blue routes. Furthermore, by turning on the flow speed controller (no. 2), the buffer can be flowed into the upper chamber for transferring the residual EXO into its collector. The purified EXOs were pumped into (pump 3) the anode chamber of EBFC-powered biosensors, which could be bound to the EXO–aptamer-modified anode via the recognition of aptamer (Apt_{CD63}). At this time, the EXOs generated a number (N_{EXOs})-dependent steric effect on the anode (Scheme 1b), ultimately resulting in a N_{EXOs}-dependent decrease in the power output (P_{max}) of EBFC-powered biosensors. After that, the collected host HeLa cells were pumped into (pump 4) the cathode chamber of EBFC-powered biosensors. Since the cathode was pre-modified with HeLa cell–aptamers (Apt_{MUC1}), thus the cells could be captured on the cathode surface and generated a number (N_{cells})-dependent steric effect. At this moment, the P_{max} of EBFC-powered biosensors further decreased with an increase in N_{cells} and exhibited a linear relationship with N_{cells}. As a result, this novel system realized the detection of EXOs and host cells and exhibited ultra-high sensitivities (EXOs: 5.59 × 10^3 particles/mL and HeLa cells: 25 cells/mL) far exceeding those of the most reported detection methods. Significantly, this integrated platform successfully monitored the growth process of EXOs and HeLa cells and revealed the growth relationship between them to reflect the growth state of tumor.

EXPERIMENTAL SECTION

Preparation of the EBFC. *Preparation of the GDL/SWCNT/AuNPs/GOD Anode.* The GDL/single-walled carbon nanotubes (SWCNTs)/AuNPs electrode was selected as the substrate electrode. We used glucose oxidase (GOD) and bilirubin oxidase (BOD) as anodic and cathodic enzymes to catalyze the electrode reactions of glucose oxidation and oxygen reduction. Also, the GDL/SWCNTs/AuNPs electrode was incubated with PBSE (1 mM) solution for 1 h. Benefiting from the strong π–π interaction between PBSE and SWCNTs, the PBSE was then immobilized on SWCNTs. After washing the electrode with water to remove the excess PBSE, the SWCNT/AuNP electrode was immersed in 0.5 mL of GOD solution (10 mg mL^{-1}) and incubated for 12 h at 4 °C. Then, the electrode was washed with water to remove the excess GOD.

Preparation of the GDL/SWCNTs/AuNPs/BOD Cathode. The GDL/SWCNTs/AuNPs/BOD cathode was prepared according to the fabrication method of the anode with BOD (20 μL, 7 mg mL^{-1}) taking the place of GOD.

This EBFC consisted of three compartments: an anode chamber, a cathode chamber, and a gas compartment. The GDL/SWCNTs/AuNPs/GOD and GDL/SWCNTs/AuNPs/BOD electrodes were used as the anode electrode and cathode electrode, respectively. Also, the gas chamber was continuously fed with purified O_2. The volume of the anode chamber and cathode chamber both was 200 μL. On connecting the anode, cathode, and gas chamber, the complete EBFC was obtained.

To determine the power output of the EBFC, we recorded the polarization curves of the EBFC from open-circuit potential to 0.0 V using a CHI 660C workstation and calculated the power density according to the formula P = UI.

Construction of EBFC-Powered Biosensors. *Preparation of the Sensing Anode of GDL/SWCNTs/AuNPs/GOD/Apt_{CD63}.* First, to modify the anode with Apt_{CD63}, 30 μL of SH-Apt_{CD63} (1 μM) was dropped on the GDL/SWCNTs/AuNPs/GOD electrode and incubated at room temperature for 5 h. Then, the Apt_{CD63}-functionalized GDL/SWCNTs/AuNPs/GOD electrode was rinsed with ultrapure water to remove the excessive aptamer. To block the nonspecific binding sites, 30 μL of 1 mM MCH was dropped on the GDL/SWCNTs/AuNPs/GOD/Apt_{CD63} electrode and incubated for 1 h at room temperature, and then, this electrode was washed with ultrapure water thoroughly to remove excessive MCH. The obtained electrode was stored at 4 °C for the future use.

Preparation of the Sensing Cathode of GDL/SWCNTs/AuNPs/BOD/Apt_{MUC1}. The fabrication method of GDL/SWCNTs/AuNPs/BOD/Apt_{MUC1} was identical to that of GDL/SWCNTs/AuNPs/GOD/Apt_{CD63}, with Apt_{MUC1} (30 μL

https://doi.org/10.1021/acs.analchem.2c01680
Anal. Chem. 2022, 94, 7722–7730

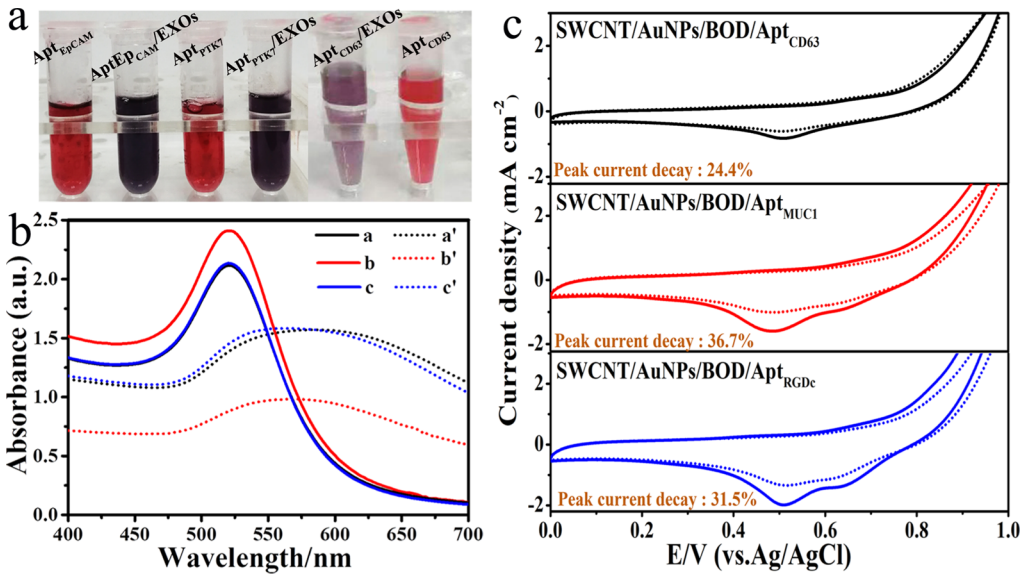

Figure 2. (a) Color and (b) UV−vis absorption spectrum changes of AuNPs induced by the aptamer−EXO interaction recorded in high-NaCl concentration solution: the AuNPs-Apt$_{EpCAM}$, AuNPs-Apt$_{CD63}$, and AuNPs-Apt$_{PTK-7}$ in the absence (a,c) and presence of EXOs (a′−c′). (c) Peak current changes at the cathode induced by the interaction between aptamer and host HeLa cells. The CV curves were recorded in the absence (dotted line) and presence of HeLa cells (dashed line), scan rate (v): 10 mV s^{-1}.

and 1 μM) taking the place of Apt$_{CD63}$. The electrode was also stored at 4 °C for further use.

By connecting the GDL/SWCNTs/AuNPs/GOD/Apt$_{CD63}$ anode, the GDL/SWCNTs/AuNPs/BOD/Apt$_{MUC1}$ cathode, and the gas chamber, we obtained the complete three-chambered EBFC-powered biosensors.

Preparation of the Flow Cell-Supported Membrane Separation System. The FMSC consisted of two chambers, which were separated by a porous AAO membrane with a pore size of 350 nm and a diameter of 2.5 cm. Also, the volumes of these two chambers were both 1.25 mL. The human serum samples (1.5 mL) containing host cancer cells and EXOs were injected into the lower chamber. Then, we adjusted the flow rate of the flow cell to 4 mL min^{-1} to generate a pressure to boost the size sieving functions of the FMSC. As such, the small EXOs were isolated from the human serum and were concentrated in the opposite chamber.

RESULTS AND DISCUSSION

Investigation of the Size-Sieving Function of the FMSC. The size-sieving function of the well-designed FMSC was first investigated. It is well known that the EXOs are smaller than 300 nm and the HeLa cells are larger than 1 μm. To ensure that the small EXOs can unimpededly pass through the separation membrane but the large cells are filtered, we selected the AAO with a pore size of 350 nm (Figures 1a and S2 and S3a) and adjusted the circulation flow rate of the FMSC to 4 mL min^{-1}. As the dark-field images showed, after circulating for an ultra-short time of 5 min, the EXOs with a size of 70−200 nm were selectively isolated from the human serum containing HeLa cells (Figure 1b,c). On the contrary, the large HeLa cells were trapped and concentrated in a cell collector without any detectable EXOs (Figure 1d). The dynamic light scattering results further confirmed that the particles larger than 300 nm were not observed in the purified EXOs and the particles smaller than 300 nm also could not be detected in the purified HeLa cells, implying the highly efficient and highly selective separation function of the FMSC (Figure 1e−g). Taken together, the well-designed FMSC realized a record-breaking EXO separation efficiency, saving 143 times time compared to the commonly used separation technique of ultracentrifugation (>12 h). What is more, the negatively stained transmission electron microscopy (TEM) images demonstrated that the purified EXOs well preserved their structural integrity (Figure S4). Also, no attached EXOs were observed on the surface of AAO after separation (Figure S3b). Taken together, the FMSC is highly efficient, highly selective, and nondestructive in the isolation of EXOs and host cells, effectively guaranteeing the detection efficiency and accuracy of the EBFC-powered biosensor integrated with it.

EXO−and Host HeLa Cell—Aptamer Screening. To design the aptamer-modified sensing anode and cathode which have high affinity for EXOs and HeLa cells, respectively, we carried out colorimetric and electrochemical experiments to screen out the optimum EXOs−aptamer cells−aptamer.[13,23] For the HeLa cell-secreted EXOs, the representative surface specific proteins which have been clearly identified were CD63, EpCAM, and PTK-7, and their binding forces (Apt$_{CD63}$, Apt$_{EpCAM}$, and Apt$_{PTK-7}$) to EXOs were investigated using the colorimetric method. These three aptamer molecules all could attach themselves on the AuNP surface through weak binding and nonspecific absorption, protecting AuNPs from aggregation in a high-salt solution. At this time, all of the aptamer/AuNP solutions exhibited an absorption peak at ∼520 nm (Figure 2a,b), while, in the presence of EXOs, the strong binding force between aptamers and EXOs dragged away the aptamers from the AuNP surface, resulting in the aggregation of AuNPs. In this context, the solution color of AuNPs-Apt$_{EpCAM}$ and AuNPs-Apt$_{PTK-7}$ changed to dark blue from red, which was consistent with the red shift of the UV−vis absorption peak, after adding EXOs. However, the solution color of AuNPs-Apt$_{CD63}$ changed to purple and the absorption intensity was lower, indicating that the EXOs caused more serious aggregation of AuNPs.

Taken together, one can draw a rational conclusion that binding force of Apt$_{CD63}$ to EXOs was the strongest among the

https://doi.org/10.1021/acs.analchem.2c01680
Anal. Chem. 2022, 94, 7722−7730

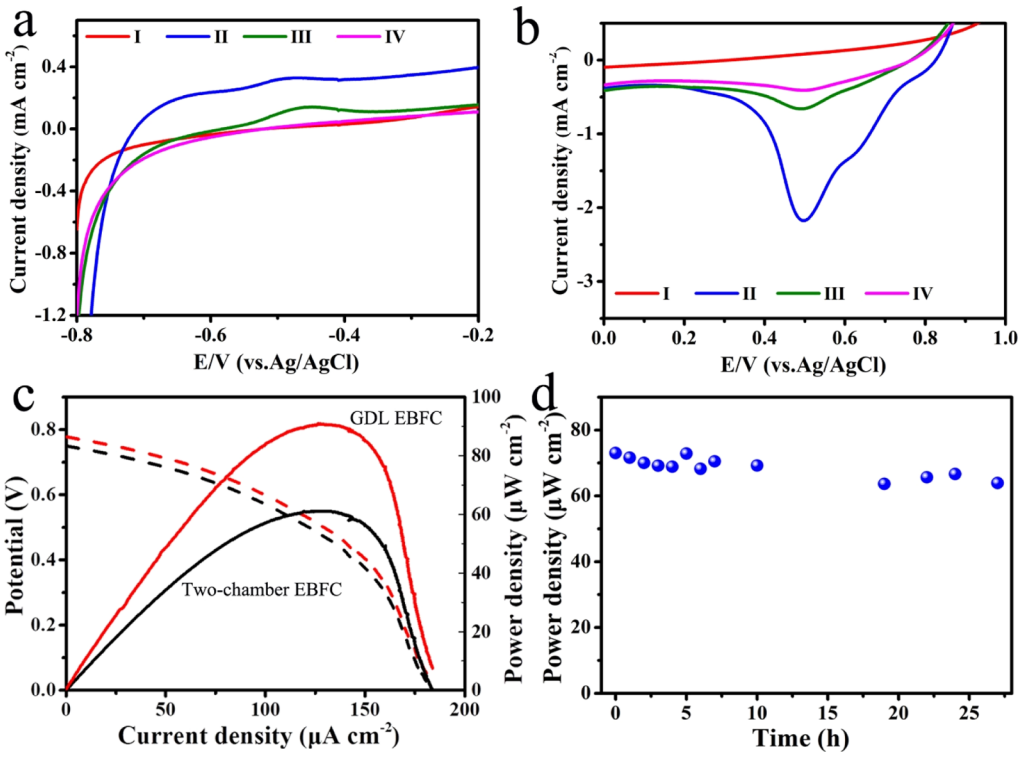

Figure 3. (a) LSV curves of the (I) SWCNTs/AuNPs, (II) SWCNTs/AuNPs/GOD, and (III) SWCNTs/AuNPs/GOD/Apt_{CD63} electrodes in the absence of EXOs and the LSV curves of (IV) SWCNTs/AuNPs/GOD/Apt_{CD63} in the presence of EXOs. (b) LSV curves of SWCNTs/AuNPs, (II) SWCNTs/AuNPs/BOD, and (III) SWCNTs/AuNPs/BOD/Apt_{MUC1} electrodes, and the LSV curves of (IV) SWCNTs/AuNPs/BOD/Apt_{MUC1} in the presence of HeLa cells. Scan rate (v): 10 mV s^{-1}. (c) Polarization curves of the EBFC equipped with the same anode and cathode recorded in the two-chamber (black) and GDL-supported three-chamber electrolytic cell (red). (d) Power density vs time curve of the EBFC-powered biosensor in cell culture medium.

three representative aptamers. Regarding HeLa cells, the representative surface makers were CD63, Mucin1 (MUC1), and arginine−glycine−aspartic−cysteine acid peptide (RGDC). To select the optimal HeLa cell−aptamer, we modified the aptamers of Apt_{CD63}, Apt_{MUC1}, and Apt_{RGDC} on the SWCNTs/AuNPs/BOD cathode and monitored the current change in the absence and presence of HeLa cells. Results revealed that the HeLa cells could be captured by the aptamer-modified cathode and hampered the cathodic reaction, resulting in an obvious decrease in peak current. However, the differences were that, in the presence of HeLa cells, the current decay rates of the SWCNTs/AuNPs/BOD/Apt_{MUC1} electrode were 36.7% while those of the SWCNTs/AuNPs/BOD/Apt_{CD63} and SWCNT/AuNPs/BOD/Apt_{RGDC} electrodes were only 24.4 and 31.5%, respectively (Figures 2c and S5). It was reasoned that Apt_{MUC1} has stronger binding force to HeLa cells compared to Apt_{CD63} and Apt_{RGDC} (Figures 2c and S5). Taken together, Apt_{CD63} and Apt_{MUC1} were selected as the aptamers to design the sensing anode and cathode to specifically detect EXOs and HeLa cells, respectively.

Construction and Feasibility of EBFC-Powered Biosensors. With the optimal EXO−aptamer (Apt_{CD63}) and HeLa cell−aptamer (Apt_{MUC1}) in hand, we tried to further design the EBFC-powered biosensors. Scheme 1b gives the detailed schematic diagram of an EBFC-powered biosensor (S1). The GOD and BOD were used as the anodic and cathodic catalysts to catalyze the glucose oxidation and oxygen reduction, respectively. Also, the SWCNT/AuNP composite was used as the electrode substrate material because it not only could work as electronic wire to accelerate the electron transfer between the enzyme and electrode but also could provide abundant sites for the immobilization of Apt_{CD63} and Apt_{MUC1} (Scheme 1b and Figure S6). As TEM and DLS tests revealed, the AuNPs were 13 nm in size and were uniformly dispersed on the SWCNTs (Figure S6a,b). Apt_{CD63} and Apt_{MUC1} were fixed on the SWCNTs/AuNPs/GOD anode and SWCNTs/AuNPs/BOD cathode, respectively. The assembly steps and sensing feasibility of the anode and cathode were verified using the linear sweep voltammetry (LSV) tests (Figure 3a,b). For the sensing anode, the oxidation current at the SWCNT/AuNP electrode at ∼−0.45 V was extremely weak (curve I) but the peak current significantly increased to as high as 0.34 mA cm^{-2} after modifying the SWCNT/AuNP electrode with GOD (curve II), confirming the high catalytic activity of immobilized GOD toward glucose oxidation. After modifying SWCNTs/AuNPs/GOD with Apt_{CD63}, the peak current slightly decreased to 0.148 mA cm^{-2} due to the steric effects of Apt_{CD63} (curve III), confirming the successful fabrication of the sensing SWCNTs/AuNPs/GOD/Apt_{CD63} anode. Noticeably, in the presence of EXOs, the peak current significantly decreased to 0.04 mA cm^{-2} (curve IV) (Figure 3a). From this, we could conclude that the EXOs could be captured by the SWCNT/AuNPs/GOD/Apt_{CD63} anode and caused the electrode current to drop, indicating the sensing feasibility of the well-designed anode for EXOs.

Regarding the HeLa cell sensing cathode, compared with the SWCNT/AuNP electrode at which hardly any reduction current was observed (curve I), the cathodic current at the SWCNT/AuNPs/BOD electrode at 0.5 V markedly increased

https://doi.org/10.1021/acs.analchem.2c01680
Anal. Chem. 2022, 94, 7722−7730

to as high as 2.19 mA cm^{-2} in O_2-saturated electrolyte (curve II). This validated the successful immobilization of BOD and its high activity toward oxygen reduction. The modification of SWCNTs/AuNPs/BOD with Apt_{MUC1} decreased the peak current to 0.68 mA cm^{-2} due to steric effects of Apt_{MUC1}, indicating the successful assembly of the sensing SWCNTs/AuNPs/BOD/Apt_{MUC1} cathode (curve III). Thanks to the high affinity of Apt_{MUC1} to HeLa cells, the HeLa cells could be captured by the sensing cathode to produce an extra blocking effect (Figure 3b). Therefore, a significant decrease in peak current (0.42 mA cm^{-2}) was observed in the presence of HeLa cells (curve IV). Results demonstrated convincingly that the well-designed cathode was able to detect the HeLa cells.

Also of note, the stability and sensitivity of EBFC-powered biosensors are inextricably linked to the performance of EBFCs. Also, one of the key factors limiting the performance of EBFC-powered biosensors is the sluggish diffusion rate of oxygen in biofluids. Given this, the gas diffusion electrode (GDL) was selected as the support electrode because it could generate an efficient three-phase interface to accelerate the oxygen diffusion rate. As expected, the P_{max} of the GDL-supported EBFC was 1.5 times higher than that of the two-chamber EBFC which used the dissolved oxygen (Figure 3c). Also, the GDL-supported EBFC could work stably for 27 h (Figure 3d). Taken together, the GDL-supported EBFC was stable and efficient enough to work as the power source and signal generator of EBFC-powered biosensors to endow the EBFC-powered biosensor with superior sensitive and stability.

Detection Performance of the EBFC-Powered Biosensor. With the successful construction of the EBFC-powered biosensor, its sensing performance was further examined. In the presence of purified EXOs, the P_{max} of the EBFC-powered biosensor decreased with the increase in the number of EXOs (N_{EXOs}) and exhibited a linear decline over a N_{EXOs} range of 1×10^3 to 1×10^7 particles (Figures 4a and S7 and S8). The relationship between the P_{max} decrease caused by EXOs ($\Delta P_{EXOs,\ max}$) and the N_{EXOs} followed a regression equation of $\Delta P_{EXOs,\ max}$ = 6.3836 log N_{EXOs}-14.0578 (R^2 = 0.98). Therefore, the P_{max} changes of the EBFC-powered biosensors could provide the quantitative information of EXOs (Figures 4b and S9). Also, the detection limit was as low as 5.59×10^3 particles/mL particles, which was significantly lower than that of the biosensors based on fluorescence (1×10^6 to 1.0×10^9)[24] and electrochemistry (1×10^5 to 13.7×10^8)[7] (Table S2). Regarding the quantitative analysis of HeLa cells, we found that, in the presence of HeLa cells, the P_{max} of the EBFC-powered biosensors decreased further. The reason was that the HeLa cells could be captured by the SWCNTs/AuNPs/BOD/Apt_{MUC1} cathode and the cathodic reaction was inhibited, ultimately resulting in a further decrease in P_{max} (Figure S10). Considering that the total P_{max} reduction of the EBFC-powered biosensor (ΔP_{max}) which had been successively incubated with EXOs and HeLa cells was the combined signals of EXOs and HeLa cells, we reasoned that the net signal of HeLa cells ($\Delta P_{HeLa,\ max}$) could be extracted by subtracting the P_{max} reduction caused by EXOs ($\Delta P_{EXOs,\ max}$) from the total P_{max} reduction (ΔP_{max}). Significantly, as Figure 4a depicts, the decrease in $\Delta P_{HeLa,\ max}$ exhibit a linear relationship with N_{cells} over a broad N_{cells} range of 5−50 000. Also, the detection limit was determined to be 25 cells/mL, lower than that of the reported tumor cells sensors (80−100 cells) shown in Table S3,[25−27] clearly proving the high sensitivity of the devised EBFC-powered biosensor toward tumor cells.

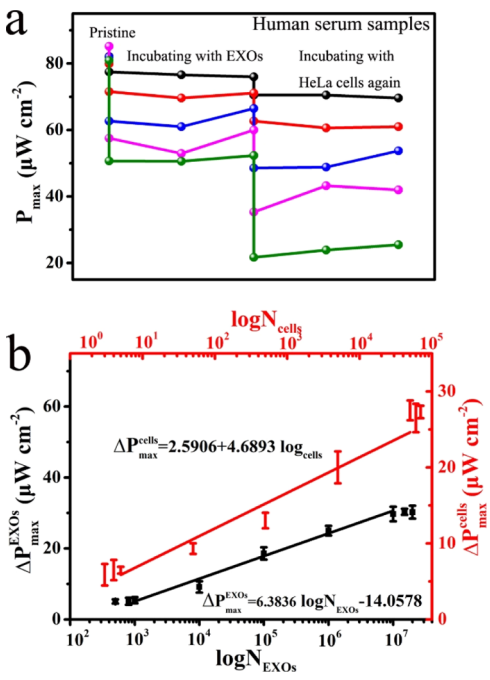

Figure 4. (a) P_{max} curves of the EBFC-powered biosensor operating in cell culture containing EXOs and later in cell culture medium containing host HeLa cells. (b) Corresponding plots of $\Delta P_{EXOs,\ max}$ vs N_{EXOs} and $\Delta P_{HeLa,\ max}$ vs N_{cells}. Error bars reflect the standard deviation of three independent measurements.

Feasibility of the FMSC- and EBFC-Powered Biosensor Coupled System in Actual Sample Analysis. Given the rapid and nondestructive EXO isolation capacity of the FMSC and the sensitive analysis capability of the EBFC-powered biosensor for EXOs and host HeLa cells, integrating the EBFC-powered biosensor with the FMSC is expected to realize the rapid isolation and continuous detection of EXOs and host HeLa cells in actual samples. To confirm this, we directly injected the human serum containing known N_{EXOs} and N_{cell} into the FMSC- and EBFC-powered biosensor coupled system. The human serum was circulated in the FMSC for 5 min, and then the purified EXOs were pumped into the anodic compartment. At this time, the P_{max} of the EBFC-powered biosensors significantly decreased. Also, the values of $\Delta P_{EXOs,\ max}$ caused by human serum containing different N_{EXOs} of 8.36×10^6 particles, 1.46×10^6 particles, and 3.76×10^5 particles were 30.28, 25.4, and 21.12 μW cm^{-2}, respectively (Figures 5a and S11). The N_{EXOs} values determined from the fitted standard curve in Figure 4b were 8.81×10^6 particles, 1.22×10^6 particles, and 3.24×10^5 particles, respectively. Therefore, the average recovery ratio of EXOs in human serum reached 84.6% (Figure 5b). After 1 hour, the purified host HeLa cells were pumped into the cathodic chamber. Compared to the EBFC-powered biosensor which had already captured EXOs at the anode, the P_{max} of the EBFC-powered biosensors further decreased. Also, the $\Delta P_{HeLa,\ max}$ values caused by 20 000, 3500, and 900 HeLa cells were determined to be 22.24, 18.88, and 16 μW cm^{-2}, respectively (Figures 5a and S12). Significantly, the detected N_{cells} values calculated from the fitted standard curve in Figure 4b were 15 488, 2971, and 748, respectively, indicating a high average recovery ratio of HeLa cells of 80.89% (Figure 5b). In addition, the P_{max} of the EBFC-powered biosensors exhibited a sequential decline after circulating the cancerous serum in the

https://doi.org/10.1021/acs.analchem.2c01680
Anal. Chem. 2022, 94, 7722−7730

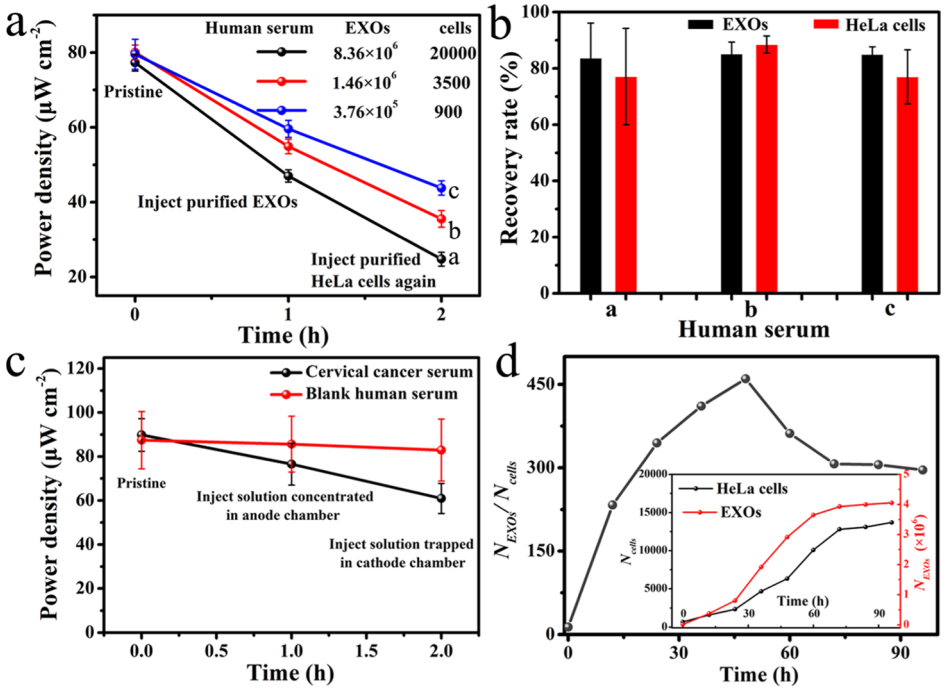

Figure 5. (a) Power output and (b) corresponding detection recovery rate of the FMSC- and EBFC-powered biosensor coupled sensing system: these tests were carried out by injecting human serum containing different concentrations of EXOs and HeLa cells into this system and then monitoring the P_{max} of the EBFC-powered biosensor via pumping in turn the purified EXOs and purified HeLa cells into the EBFC-powered biosensor system. (c) Interference test: the P_{max} change of the EBFC-powered biosensor induced by cervical cancer serum (black) and blank serum (red). (d) Growth relationship between EXOs and host HeLa cells. The inset represents the growth curves of EXOs and HeLa cells.

FMSC and successively pumping the solutions in the EXO collector and cell collector EBFC-powered biosensor coupled system (Figures 5c and S13). In contrast, no obvious P_{max} change was discovered when the FMSC- and EBFC-powered biosensor coupled system was fed with the serum derived from healthy people (Figures 5c and S14). This corroborated the detection specificity of this EBFC-powered biosensor. Taken together, the devised platform integrated by FMSC- and EBFC-powered biosensors holds great potential in rapid isolating and continuously detecting EXOs and host cancer cells.

Since the EBFC-powered biosensor could provide continuous signals, we reason that this coupled system was able to monitor the growth of EXOs and host cells to reveal the detailed growth relationship between them. To test this, we fed this system with the HeLa cell culture media cultured for different times and recorded the corresponding P_{max} changes. Also, the N_{EXOs} and N_{cells} values at different time points could be calculated from to the standard curves in Figure 4b. As shown in Figure 5d, the HeLa cells were at their early cell proliferation stage in the initial 20 h due to the slow proliferation rate. It is worth noting that, in this period, the N_{EXOs} secreted by HeLa cells also was low; however, the amount ratio of N_{EXOs} and N_{cells} increased sharply. As time went by, the HeLa cells grew rapidly during 24−72 h, indicating that the HeLa cells were in the logarithmic phase. Yet, the N_{EXOs}/N_{cells} cells kept increasing during 24−48 h but started to fall after 48 h. The above results corroborated that the FMSC- and EBFC-powered biosensor coupled system was able to provide accurate information about the growth of EXOs and the host cancer cells. A deeper conclusion was that the ability of HeLa cells to secrete EXOs was strong at the proliferation stage and during the early logarithmic phase but began to decay during the late logarithmic phase. Therefore, the absolute signals of EXOs and cancer cells can only prove the occurrence of tumor. Significantly, the growth relationship between EXOs and host cancer cells can provide in depth the growth status of tumor cells, which provides guidance information for determining the state of tumor and can further guide optimization of treatment protocols.

CONCLUSIONS

In summary, a time-saving and highly integrated platform has been developed to nondestructively isolate and continuously detect EXOs and their host cells via integrating the dual-channel EBFC-powered biosensor with a flow cell-supported membrane separation device. This system isolated EXOs and host cancer cells from human serum within 5 min, cutting the 99.3 percentage of time cost compared to ultracentrifugation. Moreover, this system successively detected EXOs and the host HeLa cells in human serum with high sensitivities (EXOs: 5.59×10^3 particles/mL and HeLa cell: 25 cells/mL), only by controlling the injection time of EXOs and host cells after the separation with the FMSC. The growth relationship between EXOs and host cancer cells has also been revealed by this integrated system, which would be beneficial to determine the growth state of tumor and guide the optimization of treatment protocols. This study not only opened a sunshine avenue to isolate and assess EXOs and host cells but also pioneered a new type for probing the potential association between the quantitative information of EXOs and tumor growth.

ASSOCIATED CONTENT

Supporting Information

The Supporting Information is available free of charge at https://pubs.acs.org/doi/10.1021/acs.analchem.2c01680.

https://doi.org/10.1021/acs.analchem.2c01680
Anal. Chem. 2022, 94, 7722−7730

SEM images of the AAO, negatively stained TEM image of EXOs isolated using the FMSC system, DLS results of the AuNPs and the zeta potential of AuNPs, SWCNT, SWCNT/PDDA, and SWCNT/AuNPs, particle size distribution and the concentration of EXOs, power output curves of the EBFC-powered biosensors in the presence of different numbers of EXOs and HeLa cells, power output curves of the FMSC- and EBFC- powered biosensor coupled system in cervical cancer serum and human serum from healthy people, and EXOs and cell detection performance of the recently reported biosensors (PDF)

AUTHOR INFORMATION

Corresponding Authors

Linlin Wang − *State Key Laboratory of Analytical Chemistry for Life Science, School of Chemistry and Chemical Engineering, Nanjing University, Nanjing 210023, P. R. China*; Email: wanglinlin@nju.edu.cn

Jun-Jie Zhu − *State Key Laboratory of Analytical Chemistry for Life Science, School of Chemistry and Chemical Engineering, Nanjing University, Nanjing 210023, P. R. China*; orcid.org/0000-0002-8201-1285; Email: jjzhu@nju.edu.cn

Jian-Rong Zhang − *State Key Laboratory of Analytical Chemistry for Life Science, School of Chemistry and Chemical Engineering, Nanjing University, Nanjing 210023, P. R. China*; Email: jrzhang@nju.edu.cn

Authors

Tajiguli Yimamumaimaiti − *State Key Laboratory of Analytical Chemistry for Life Science, School of Chemistry and Chemical Engineering, Nanjing University, Nanjing 210023, P. R. China*; orcid.org/0000-0003-1908-3590

Qiwen Su − *State Key Laboratory of Analytical Chemistry for Life Science, School of Chemistry and Chemical Engineering, Nanjing University, Nanjing 210023, P. R. China*

Rong-bin Song − *School of Ecology and Environment, Zhengzhou University, Zhengzhou 450001, P. R. China*

Yan Gao − *State Key Laboratory of Analytical Chemistry for Life Science, School of Chemistry and Chemical Engineering, Nanjing University, Nanjing 210023, P. R. China*

Sha Yu − *State Key Laboratory of Analytical Chemistry for Life Science, School of Chemistry and Chemical Engineering, Nanjing University, Nanjing 210023, P. R. China*

Tingting Tan − *Department of Laboratory Medicine, Nanjing Drum Tower Hospital, The Affiliated Hospital of Nanjing University Medical School, Nanjing 210008, P. R. China*

Complete contact information is available at: https://pubs.acs.org/10.1021/acs.analchem.2c01680

Author Contributions

T.Y. and L.-L.W. conceived and designed the experiments. T.Y. performed all experimental work. Y.G. contributed to the dark-field images. T.Y. and L.-L.W. analyzed the data. L.-L.W. and T.Y. wrote the original draft. L.-L.W., R.-B.S., J.-R.Z., and J.-J.Z. revised the draft elaborately. All authors discussed the results and commented on the article.

Notes

The authors declare no competing financial interest.

ACKNOWLEDGMENTS

We gratefully acknowledge the financial support from the National Natural Science Foundation of China (22004060 and 22074062). We also thank the financial support from the Shandong Provincial Natural Science Foundation (ZR2020ZD37) and the State Key Laboratory of Analytical Chemistry for Life Science (SKLACLS2108). L. L.W. is also thankful for financial support from the Natural Science Foundation of Jiangsu Province (BK20200305).

REFERENCES

(1) Kalluri, R.; LeBleu, V. S. *Science* **2020**, *367*, No. eaau6977.
(2) Zhao, J.; Liu, C.; Li, Y.; Ma, Y.; Deng, J.; Li, L.; Sun, J. *J. Am. Chem. Soc.* **2020**, *142*, 4996−5001.
(3) Marsh, M.; van Meer, G. *Science* **2008**, *319*, 1191−1192.
(4) Mathew, D. G.; Beekman, P.; Lemay, S. G.; Zuilhof, H.; Le Gac, S.; van der Wiel, W. G. *Nano Lett.* **2020**, *20*, 820−828.
(5) Im, H.; Shao, H.; Park, Y. I.; Peterson, V. M.; Castro, C. M.; Weissleder, R.; Lee, H. *Nat. Biotechnol.* **2014**, *32*, 490−495.
(6) Lin, B.; Tian, T.; Lu, Y.; Liu, D.; Huang, M.; Zhu, L.; Zhu, Z.; Song, Y.; Yang, C. *Angew. Chem., Int. Ed.* **2021**, *60*, 7582−7586.
(7) Yang, L.; Yin, X.; An, B.; Li, F. *Anal. Chem.* **2021**, *93*, 1709−1716.
(8) Kharaziha, P.; Ceder, S.; Li, Q.; Panaretakis, T. *Biochim. Biophys. Acta, Rev. Cancer* **2012**, *1826*, 103−111.
(9) Muralidharan-Chari, V.; Clancy, J. W.; Sedgwick, A.; D'Souza-Schorey, C.; Microvesicles, C. *Cell Sci.* **2010**, *123*, 1603−1611.
(10) Nabet, B. Y.; Qiu, Y.; Shabason, J. E.; Wu, T. J.; Yoon, T.; Kim, B. C.; Benci, J. L.; DeMichele, A. M.; Tchou, J.; Marcotrigiano, J.; Minn, A. J. *Cell* **2017**, *170*, 352−366.
(11) Matei, I.; Kim, H. S.; Lyden, D. *Cell* **2017**, *170*, 223−225.
(12) Zhai, L.-Y.; Li, M.-X.; Pan, W.-L.; Chen, Y.; Li, M.-M.; Pang, J.-X.; Zheng, L.; Chen, J.-X.; Duan, W.-J. *ACS Appl. Mater. Interfaces* **2018**, *10*, 39478−39486.
(13) Jiang, Y.; Shi, M.; Liu, Y.; Wan, S.; Cui, C.; Zhang, L.; Tan, W. *Angew. Chem., Int. Ed.* **2017**, *56*, 11916−11920.
(14) Mori, K.; Hirase, M.; Morishige, T.; Takano, E.; Sunayama, H.; Kitayama, Y.; Inubushi, S.; Sasaki, R.; Yashiro, M.; Takeuchi, T. *Angew. Chem., Int. Ed.* **2019**, *58*, 1612−1615.
(15) Yoshioka, Y.; Kosaka, N.; Konishi, Y.; Ohta, H.; Okamoto, H.; Sonoda, H.; Nonaka, R.; Yamamoto, H.; Ishii, H.; Mori, M.; Furuta, K.; Nakajima, T.; Hayashi, H.; Sugisaki, H.; Higashimoto, H.; Kato, T.; Takeshita, F.; Ochiya, T. *Nat. Commun.* **2014**, *5*, 3591.
(16) Vargas, E.; Teymourian, H.; Tehrani, F.; Eksin, E.; Sánchez-Tirado, E.; Warren, P.; Erdem, A.; Dassau, E.; Wang, J. *Angew. Chem., Int. Ed.* **2019**, *58*, 6376−6379.
(17) Fan, S.; Liang, B.; Xiao, X.; Bai, L.; Tang, X.; Lojou, E.; Cosnier, S.; Liu, A. *J. Am. Chem. Soc.* **2020**, *142*, 3222−3230.
(18) Wang, F.-T.; Wang, Y.-H.; Xu, J.; Huang, K.-J.; Liu, Z.-h.; Lu, Y.-f.; Wang, S.-y.; Han, Z.-w. *Nano Energy* **2020**, *68*, 104310.
(19) Wang, L.; Shao, H.; Lu, X.; Wang, W.; Zhang, J.-R.; Song, R.-B.; Zhu, J.-J. *Chem. Sci.* **2018**, *9*, 8482−8491.
(20) Sun, M.; Xin, T.; Ran, Z.; Pei, X.; Ma, C.; Liu, J.; Cao, M.; Bai, J.; Zhou, M. *ACS Sens.* **2021**, *6*, 275−284.
(21) Wang, L.-L.; Shao, H.-H.; Wang, W.-J.; Zhang, J.-R.; Zhu, J.-J. *Nano Energy* **2018**, *44*, 95−102.
(22) Xiao, X.; McGourty, K. D.; Magner, E. *J. Am. Chem. Soc.* **2020**, *142*, 11602−11609.
(23) Gai, P.-P.; Ji, Y.-S.; Wang, W.-J.; Song, R.-B.; Zhu, C.; Chen, Y.; Zhang, J.-R.; Zhu, J.-J. *Nano Energy* **2016**, *19*, 541−549.
(24) He, D.; Ho, S.-L.; Chan, H.-N.; Wang, H.; Hai, L.; He, X.; Wang, K.; Li, H.-W. *Anal. Chem.* **2019**, *91*, 2768−2775.
(25) Li, Z.; Wang, G.; Shen, Y.; Guo, N.; Ma, N. *Adv. Funct. Mater.* **2018**, *28*, 1707152.
(26) Cao, J.; Zhao, X.-P.; Younis, M. R.; Li, Z.-Q.; Xia, X.-H.; Wang, C. *Anal. Chem.* **2017**, *89*, 10957−10964.

(27) Yin, X.; Chen, B.; He, M.; Hu, B. *Anal. Chem.* **2020**, *92*, 10308−10315.

https://doi.org/10.1021/acs.analchem.2c01680
Anal. Chem. 2022, 94, 7722−7730